mathematics

MDPI

Article

Graphene Twistronics: Tuning the Absorption Spectrum and Achieving Metamaterial Properties

Ammar Armghan [1,*], Meshari Alsharari [1,*], Khaled Aliqab [1], Osamah Alsalman [2], Juveriya Parmar [3,4] and Shobhit K. Patel [4]

[1] Department of Electrical Engineering, College of Engineering, Jouf University, Sakaka 72388, Saudi Arabia
[2] Department of Electrical Engineering, College of Engineering, King Saud University, P.O. Box 800, Riyadh 11421, Saudi Arabia
[3] Department of Mechanical and Materials Engineering, University of Nebraska-Lincoln, 1400 R St., Lincoln, NE 68588, USA
[4] Department of Computer Engineering, Marwadi University, Rajkot 360003, India
* Correspondence: aarmghan@ju.edu.sa (A.A.); mmaalsharari@ju.edu.sa (M.A.)

Abstract: Graphene twistronics using multilayer graphene is presented in such a way that it provides a metamaterial effect. This manuscript also analyzes the prediction of behavior using machine learning. The metamaterial effect is achieved by twisting the graphene layers. Graphene twistronics is a new concept for changing the electrical and optical properties of bilayer graphene by applying a small angle twist between the layers. The angle twists of 5°, 10°, and 15° are analyzed for the proposed graphene twistronics design. Tuning in the absorption spectrum is achieved by applying small twists to the angles of the bilayer graphene. Results in the form of absorption, conductivity, permeability, permittivity, and impedance are presented for different twist angles. The twisted graphene layers also demonstrate negative permittivity and negative permeability, similar to metamaterials. These negative refraction properties of graphene twistronics provide flexibility and transparency, which can be applied in photovoltaic applications. Machine-learning-based regression models are used to reduce the simulation time and resources. The results show that a regression model can reliably estimate intermediate wavelength absorption values with an R^2 of 0.9999.

Keywords: twistronics; photonics; graphene; metamaterial; absorption; tuning

MSC: 78-10; 78-04; 00A06

Citation: Armghan, A.; Alsharari, M.; Aliqab, K.; Alsalman, O.; Parmar, J.; Patel, S.K. Graphene Twistronics: Tuning the Absorption Spectrum and Achieving Metamaterial Properties. *Mathematics* **2023**, *11*, 1579. https://doi.org/10.3390/math11071579

Academic Editor: Nikolaos L. Tsitsas

Received: 6 February 2023
Revised: 20 March 2023
Accepted: 20 March 2023
Published: 24 March 2023

1. Introduction

Graphene is a monolayer sheet of graphite with a a honeycomb structure. Graphene material has high conductivity with electric and optical properties [1]. Extensive research is currently being performed on graphene material by various research groups due to its unique properties and applicability. Graphene is used as a sensing material in biosensor design to sense hemoglobin and urine biomolecules [2,3]. Graphene can also be used in the design of solar absorbers to increase their absorbing capacity. Graphene superstructure Bragg gratings can be an effective reflective surface for use in photovoltaic applications. Metal–graphene nanostructures can be synthesized and used in photocatalysis [4]. Graphene can also deliver transparent features which are applicable in the construction of transparent structures [5,6]. Graphene is also used to increase the absorption of solar absorbers and THz absorbers [7,8]. Graphene material enhances the absorption of the THz absorber so that perfect absorption is achieved by the absorber [9]. The perfect absorption of the THz absorbers can also be tuned by varying the graphene chemical potential [10,11]. Solar cells and solar absorbers also use graphene as a component for improving the conversion of solar radiation to electricity and heat energy, respectively [12–14]. Graphene-based antennas are also currently used in many applications as graphene can be used to reconfigure the

frequency and radiation pattern of an antenna [15,16]. Graphene material is also used to explain the mathematical aspects of surface plasmon resonance [17,18]. The optimization of the metamaterial structures is also achieved by applying parametric optimization methods. These features of graphene make it a valid candidate for futuristic research approaches.

Twistronics involves changing the electrical properties of 2D materials by a slight change in the angle between two layers of these materials [19]. This new concept can be used with 2D materials such as graphene because of its electrical and optical properties. Graphene twistronics is a new development in graphene nanostructures in which two graphene layers are placed at different angles to change the behavior of the light falling onto them. Graphene twistronics can also be applied in van der Waals structures in which small angle changes between the layers are used to modify the van der Waals structural properties [20]. Twisted layers of graphene provide changes in properties such as superconductivity, absorption, reactivity, decoupling, and van Hove singularities [21–24]. With its magic angle twist and variation in superconductivity, twistronics can be applicable in many photovoltaic applications [25]. MoS_2 is another material that is used in twistronics. The twist in the angle between two MoS_2 layers can continuously change the bandgap of the material [26]. The twist in a bilayer 2D material can tailor the photonic response when light interacts with it [27]. The magic angle twist in a bilayer graphene material can be used as a novel phenomenon for improvement in photonic structures [28]. A review of these excitonic devices is presented in [29]. These devices demonstrate the van der Walls interaction, which is used in converting valleytronics to twistronics. Graphene material can be used for designing twisted blade structures for mechanical applications [30]. Several resonance conditions have been exploited to achieve acoustic metamaterials, such as Minnaert resonance [31]. A plasmon resonance-based nanorod structure was analyzed, and the asymptotic formulae were derived using the localized resonance for the construction of negative materials [32]. While studying the plasmonic resonance of photonic crystals, the researcher concluded that the electron relaxation time/filling factor could be controlled [33]. In these works, the metamaterial devices of core–shell structures can also induce invisibility and transparency due to the so-called anomalous localized resonance [34]. The optical properties of different two dimensional materials such as MoS2/ZnO are discussed in [35]. The optical properties of dichacogenides and graphene materials are discussed in [36].

The bilayer graphene material twist can be used for different photonic applications. Our aim here is to design graphene twistronics to tune the absorption waveform. This tuning is achieved by changing the small angle between the two graphene layers. The tuning is observed for 5°, 10°, and 15° angle differences between the two layers. The graphene twistronics design, its results, and conclusions are discussed in the following sections.

2. Graphene Twistronics Design

A graphene twistronics design with bilayer graphene placed on a silicon dioxide substrate is presented in Figure 1. The two monolayer graphene sheets were placed above this substrate at different angles (θ°). The angle between the graphene layers was observed for 0°, 5°, 10°, and 15°. The top view of the design, with an angled twist of θ°, is shown in Figure 1c. The angle was slowly increased to determine the effect of the twist. The area of the silica material was kept at 25 × 25 μm^2. The graphene layer area and width were 25 × 25 μm^2. The thickness of the silica was 0.6 μm. The thickness of a single-layer graphene sheet was 0.34 nm. Furthermore, an xy plane periodic boundary condition with light coming from the z-direction was applied, and a Delaunay Tessellation tetrahedral meshing condition was used for the simulation. The simulations were carried out using COMSOL Multiphysics software [37]. The main aim of the proposed design was to observe the tuning in the spectrum using graphene twistronics. Calculations of the reflectance, absorption, and graphene conductivity are presented in this section.

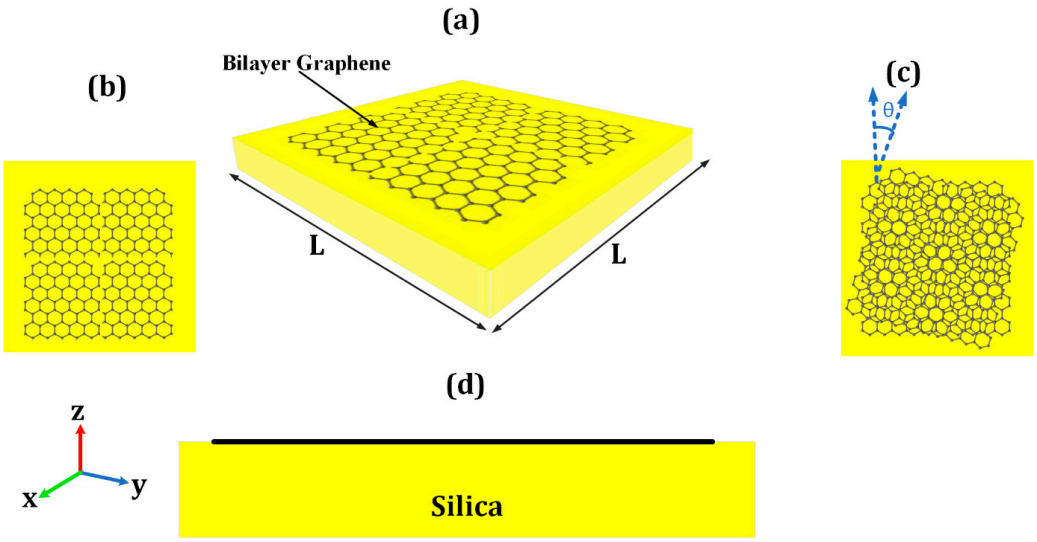

Figure 1. Graphene twistronics: (**a**) three-dimensional model of bilayer graphene placed on silica substrate without twist; (**b**) bilayer graphene without twist placed on silica substrate (top view); (**c**) bilayer graphene with twist angle θ° placed over silica substrate (top view); (**d**) bilayer graphene place on silica substrate (side view), L = 25 μm.

Graphene monolayer sheet design and conductivity:

The graphene model has been investigated numerically in different studies in the literature. The numerical modeling of graphene is presented in [38]. The surface plasmon resonance-based graphene model is presented in [39]. Monolayer graphene in cylindrical configurations is presented in [40]. Graphene conductivity is presented in the following equations: Equations (1)–(6). The parameters are presented in [41]. Here, we have utilized the formulation resulting from Kubo's formula [42]. The dependence of graphene's potential on its conductivity is presented below.

Here, we have utilized the formulation resulting from Kubo's formula [42]:

$$\sigma\ (\omega, \mu_c, \Gamma,\ \mathrm{T}) = \frac{je^2(\omega - j2\Gamma)k_B T}{\pi\hbar^2}\left[\frac{1}{(\omega - j2\Gamma)^2}\int_0^\infty \varepsilon\left(\frac{df_d(\varepsilon)}{d\varepsilon} - \frac{df_d(-\varepsilon)}{d\varepsilon}\right)d\varepsilon - \int_0^\infty \frac{f_d(-\varepsilon) - f_d(\varepsilon)}{(\omega - j2\Gamma)^2 - 4\left(\frac{\varepsilon}{\hbar}\right)^2}d\varepsilon\right] \quad (1)$$

where $-$e is the charge of an electron, $\hbar = \mathrm{h}/2\pi$ is the reduced Planck's constant, $f_d(\varepsilon) = \left(e^{(\varepsilon-\mu_c)/k_B T} + 1\right)^{-1}$ is the Fermi–Dirac distribution, and kB is the Boltzmann constant. We assume that no external magnetic field is present; therefore, the local conductivity is isotropic (i.e., there is no Hall conductivity). The first term in Equation (1) is due to intraband contributions, and the second term is due to to interband contributions. For an isolated graphene sheet, the chemical potential μ_c is determined by the carrier density ns:

$$n_s = \frac{2}{\pi\hbar^2 v_F^2}\int_0^\infty \varepsilon[f_d(\varepsilon) - f_d(\varepsilon + 2\mu_c)]d\varepsilon \quad (2)$$

where vF $\approx 9.5 \times 10^5$ m/s is the Fermi velocity. The carrier density can be controlled by the application of a gate voltage and/or chemical doping. For the undoped, ungated case at T = 0 K, ns = μ_c = 0. The intraband term in Equation (1) can be evaluated as:

$$\sigma_{intra}(\omega, \mu_c, \Gamma,\ \mathrm{T}) = \frac{-je^2 k_B T}{\pi\hbar^2\ (\omega - j2\Gamma)}\left(\frac{\mu_c}{k_B T} + 2\ \ln\left(e^{\frac{\mu_c}{k_B T}} + 1\right)\right) \quad (3)$$

The interband conductivity can be approximated for kBT << μ_c, as

$$\sigma_{inetr}(\omega, \mu_c, \Gamma, 0) = \frac{-je^2}{4\pi\hbar} \ln\left(\frac{2|\mu_c| - (\omega - j2\Gamma)\hbar}{2|\mu_c| + (\omega - j2\Gamma)\hbar}\right) \tag{4}$$

$$\sigma_s = \sigma_{inter} + \sigma_{intra} \tag{5}$$

$$\varepsilon(\omega) = 1 + \frac{\sigma_s}{\varepsilon_0 \omega \Delta} \tag{6}$$

A single-layer graphene model was presented in Equations (1)–(6), and a twisted graphene mathematical model is derived in Equations (7)–(25).

A low-energy Hamiltonian continuum model with two single-layer Dirac–Hamiltonian terms refers to two isolated graphene sheets, and hopping between two layers is referred to using a tunneling term [43,44]:

$$h_k(\theta) = -vk \begin{bmatrix} 0 & e^{i(\theta_k - \theta)} \\ e^{-i(\theta_k - \theta)} & 0 \end{bmatrix} \tag{7}$$

$$T_{kp'}^{\alpha\beta} = \langle \Psi_{k\alpha}^{(1)} | H_T | \Psi_{p'\beta}^{(2)} \rangle \tag{8}$$

$$|\Psi_{k\alpha}^{(1)}\rangle = \frac{1}{\sqrt{N}} \sum_R e^{ik(R+\tau_a)} |R + \tau_a\rangle \tag{9}$$

$$|\Psi_{p\beta}^{(1)}\rangle = \frac{1}{\sqrt{N}} \sum_{R'} e^{ip(R'+\tau'_\beta)} |R' + \tau'_\beta\rangle \tag{10}$$

Here, $\tau_a = 0$ and $\tau_\beta = \tau$. R represents the summed-up triangular Bravais lattice. Substituting Equations (7) and (8) in Equation (6):

$$\langle R + \tau_a | H_T | R' + \tau'_\beta \rangle = t(R + \tau_a - R' - \tau'_\beta) \tag{11}$$

$$T_{kp'}^{\alpha\beta} = \sum_{G_1 G_2} \frac{t_{\overline{k}+G_1}}{\Omega} e^{i[G_1\tau_a - G_2(\tau_\beta - \tau)G'_2 d]} \delta_{\overline{k}+G_1, \overline{p}'+G'_2} \tag{12}$$

where $G'_2 = MG_2$

$$T^{\alpha\beta}(r) = w \sum_{j=1}^{3} \exp(-iq_j.r) T_j^{\alpha\beta} \tag{13}$$

where $w = t_{k_D}/\Omega$

$$T_1 = \begin{pmatrix} 1 & 1 \\ 1 & 1 \end{pmatrix},\ T_1 = e^{-i\varsigma^{(2)'}.d} \begin{pmatrix} e^{-i\phi} & 1 \\ e^{i\phi} & e^{-i\phi} \end{pmatrix} \tag{14}$$

$$T_3 = e^{-i\varsigma^{(2)'}.d} \begin{pmatrix} e^{-i\phi} & 1 \\ e^{i\phi} & e^{-i\phi} \end{pmatrix} \tag{15}$$

$$\mathcal{H}_k = \begin{bmatrix} h_k\left(\frac{\theta}{2}\right) & T_b & T_{tr} & T_{tl} \\ T_b^{\mathfrak{k}} & h_{k_b}\left(-\frac{\theta}{2}\right) & 0 & 0 \\ T_{tr}^{\mathfrak{k}} & 0 & h_{k_{tr}}\left(-\frac{\theta}{2}\right) & 0 \\ T_{tl}^{\mathfrak{k}} & 0 & 0 & h_{k_{tl}}\left(-\frac{\theta}{2}\right) \end{bmatrix} \tag{16}$$

The renormalized velocity $v^* = \partial_k c_k^*|_{k=0}$; consider k = 0

$$\Psi_j = -h_j^{-1} T_j^{\mathfrak{k}} \Psi_0 \tag{17}$$

as

$$T_j h_j^{-1} T_j^{\mathfrak{k}} = 0 \tag{18}$$

The equation for the Ψ_0 spinor is $h_0\Psi_0 = 0$; given that $|\Psi_0^{(j)}| = 1$, the wave eq. can be normalized by $|\Psi|^2 = 1 + 6\alpha^2$.

The effective Hamiltonian matrix is then provided as:

$$\left\langle \Psi^{(i)} | \mathcal{H}_k^{(1)} | \Psi^{(j)} \right\rangle = \frac{-v}{1+6\alpha^2} \Psi_0^{(i)\mathfrak{k}} [\sigma.k + w^2 \sum_j T_j h_j^{-1\mathfrak{k}} \sigma.k h_j^{-1\mathfrak{k}} T_j] \Psi_0^{(j)} = -v^* \Psi_0^{(i)\mathfrak{k}} \sigma.k \Psi_0^{(j)} \tag{19}$$

$$\frac{v^*}{v} = \frac{1-3\alpha^2}{1+6\alpha^2} \tag{20}$$

The Hamiltonian is equivalent to a single-layer graphene Hamiltonian, and using Kubo formula, we can find:

$$\sigma_{CF} = \frac{4e^2}{\pi} \sum_{k\mu} |\langle \Psi_k | v_{CF}^x | \Psi_j \rangle|^2 [\mathrm{Im}\{G_{k\mu}^r(C_F)\}]^2 \tag{21}$$

where

$$v_{CF}^x = -v \begin{pmatrix} \sigma_x & 0 & 0 & 0 \\ 0 & -\sigma_x & 0 & 0 \\ 0 & 0 & -\sigma_x & 0 \\ 0 & 0 & 0 & -\sigma_x \end{pmatrix} \tag{22}$$

The valence band can be neglected for an electron-doped system.

$$\sigma_{CF} \approx e^2 g \tau v^*(C_F) \int \frac{d\theta_k}{2\pi} |\langle \Psi_{k\mu} | v_{CF}^x | \Psi_{k\mu} \rangle|^2 \tag{23}$$

The vertex function is given as:

$$|\langle \Psi_k | v_{CF}^x | \Psi_j \rangle| = v_{CF} \cos\theta_k \tag{24}$$

where $v_{CF} = v\left(1+3\alpha^2\right)/\left(1+6\alpha^2\right)$.

The counterflow conductivity then can be derived as:

$$\sigma_{CF} = \sigma_0 \left(\frac{v_{CF}}{v^*} \right) \tag{25}$$

where $\sigma_0 \sim e^2 C_F \tau/\pi$ is the single-layer isolated graphene sheet.

The permittivity and permeability equations of the metasurfaces are presented in Equations (26)–(30). These parameters are obtained from the impedance and the refractive index, as presented in the equations [45]:

$$z = \pm \sqrt{\frac{(1+S_{11})^2 - S_{21}{}^2}{(1-S_{11})^2 - S_{21}{}^2}} \tag{26}$$

$$e^{ink_0 d} = \frac{S_{21}}{1 - S_{11}\frac{z-1}{z+1}} \tag{27}$$

$$n = \frac{1}{k_0 d} \left[\left\{ \left[\ln(e^{ink_0 d}) \right]'' + 2m\pi \right\} - i \left[\ln(e^{ink_0 d}) \right]' \right] \tag{28}$$

$$\varepsilon = \frac{n}{z} \tag{29}$$

$$\mu = nz \tag{30}$$

The reflectance and absorption of the structure has a strong relevance to the angle of incidence, which is presented in the following Equations (31)–(37) [41,46]:

$$r(\omega,\theta_i) = \frac{\cos\theta_i \prod_{00}(\omega,\theta_i)}{2ick^2 + \omega\cos\theta_i \prod_{00}(\omega,\theta_i)} \tag{31}$$

$$\sigma_{||}(\omega,k) = X = -i\,\frac{\omega}{4\pi\hbar k^2}\prod_{00}(\omega,k) \tag{32}$$

$$r(\omega,\theta_i) = \frac{2\pi\cos\theta_i\sigma_{||}(\omega,k)}{c + 2\pi\cos\theta_i\sigma_{||}(\omega,k)} \tag{33}$$

$$\mathcal{R}(\omega,\theta_i) = |r(\omega,\theta_i)|^2 \tag{34}$$

$$\mathcal{R}(\omega,\theta_i) = \frac{4\pi^2\cos^2\theta_i\left[\mathrm{Re}^2X + \mathrm{Im}^2X\right]}{[c + 2\pi\cos\theta_i\mathrm{Re}X]^2 + 4\pi^2\cos^2\theta_i\mathrm{Im}^2X} \tag{35}$$

$$\begin{aligned}\mathcal{R}(\omega) &= \mathcal{R}(\omega,0)\\ &= \frac{4\pi^2\left[\mathrm{Re}^2\sigma(\omega)+\mathrm{Im}^2\sigma(\omega)\right]}{[c+2\pi\mathrm{Re}\sigma(\omega)]^2+4\pi^2\mathrm{Im}^2\sigma(\omega)}\end{aligned} \tag{36}$$

$$A(\omega) = 1 - \mathcal{R}(\omega) - T(\omega) \tag{37}$$

Since the suggested structure operates in the optical wavelength, it is essential to have a firm grasp on the options available to you when developing metal–insulator–metal (MIM) for ultraviolet (UV)–visible (VIS)—near infrared (NIR) and dielectric layers with a high temperature stability and correct optical properties. In this three-layer structure, tungsten, as a metal, has a high temperature stability (3422 °C), and is thus the best choice for a base metal for an MIM. SiO_2 acts as a dielectric layer between the resonator and the metal layer, reducing the structure's resonance frequency while still allowing for adequate capacitance and inductance coupling [47], The structure is helped along the path to greater absorbance and a wider bandwidth by the low refractive index. The high melting point of SiO2 (1710 °C) will also aid in the structure's resistance to the intense electromagnetic waves produced by the sun.

The graphene twistronics modeling was achieved using the Kubo formula defined in Equations (1)–(6). In the process, the bilayer graphene sheets were designed. Furthermore, the process of graphene deposition on an insulator medium is a tough process, and is recently a process in which the graphene can be deposited on a glass substrate at a rate of 34 nm in 5 min. This process can be followed for the fabrication of the proposed structure. Later, the quantities provided in Equations (7)–(11) are utilized for calculations of the impedance, refractive index, permittivity, and permeability. The proposed model was defined as two-port network; for this, the S_{11} and S_{21} were calculated, and the rest of the quantities were calculated from these two values. Furthermore, the twist in the bilayer graphene model was introduced to achieve higher results; these results were then calculated to identify the highest-performing twist angle. This process is described in the flowchart in Figure 2.

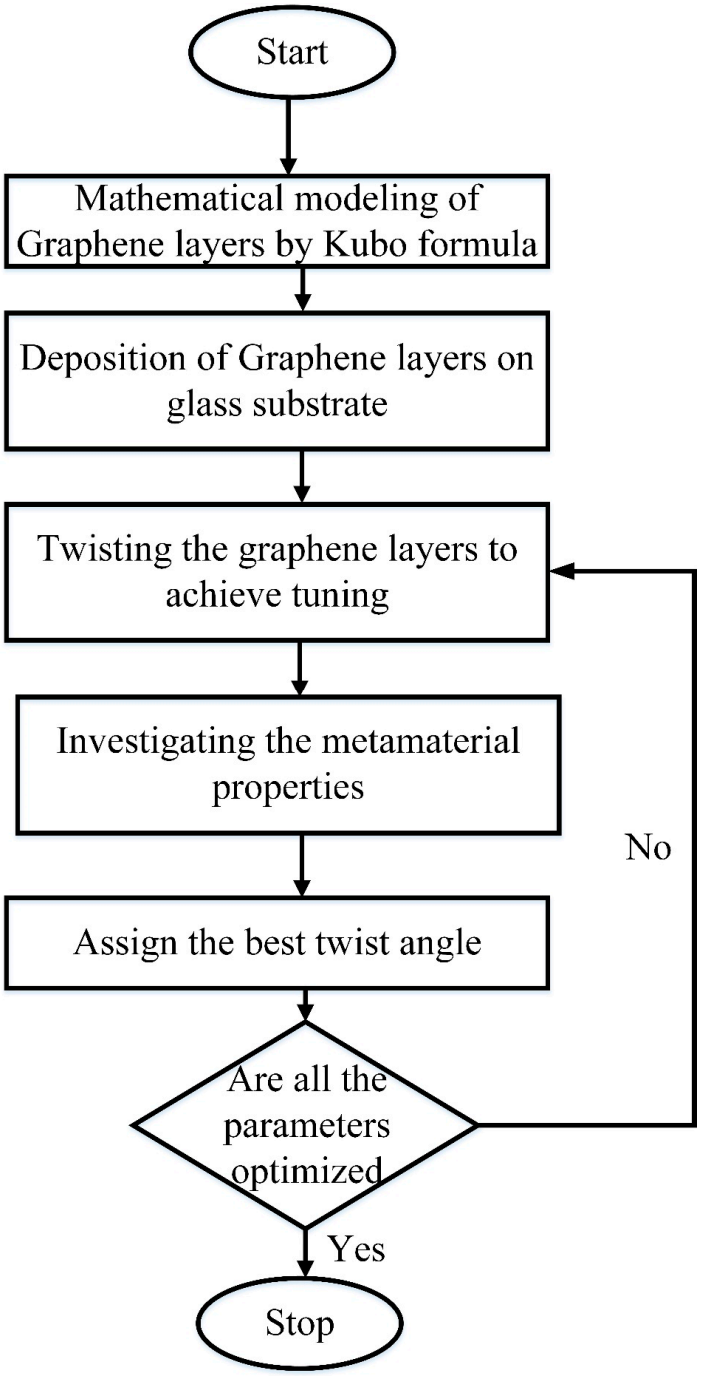

Figure 2. Flowchart describing the graphene twistronics modeling and investigation methodology for achieving the optical properties.

3. Results and Discussion

The graphene twistronics design is shown in Figure 1. The design of graphene twistronics with an angled twist between the two layers was analyzed using COMSOL Multiphysics. The analyzed results, such as the absorption, permittivity, permeability, conductivity, and impedance, are provided in Figures 3–6. The response for the twist angle of 5° is provided in Figure 3. The absorption response for this 5° twist is provided in Figure 3a. The absorption response was more than 60% for the whole wavelength range observed. The peak absorption was achieved at 1.2 µm. The conductivity response for this 5° twist is provided in Figure 3b. The conductivity response is provided in real and imaginary forms. The conductivity is on the higher side because of the graphene. The impedance, permeability,

and permittivity values are provided in Figure 3c–e, respectively. The permittivity and permeability demonstrated negative real values for some wavelengths, which created negative refraction, just like the metamaterials. The negative metamaterial propoerties were visible at 0.85 µm, 1.05 µm, and 1.39 µm. A similar effect was produced using twisted graphene nanoribbons in a recently published study [27]. This behavior was observed due to the twisting bilayer graphene material. We also observed whether the effect was noticed in increased angles or not, and its response is provided in Figures 4 and 5 for twist angles 10° and 15°, respectively.

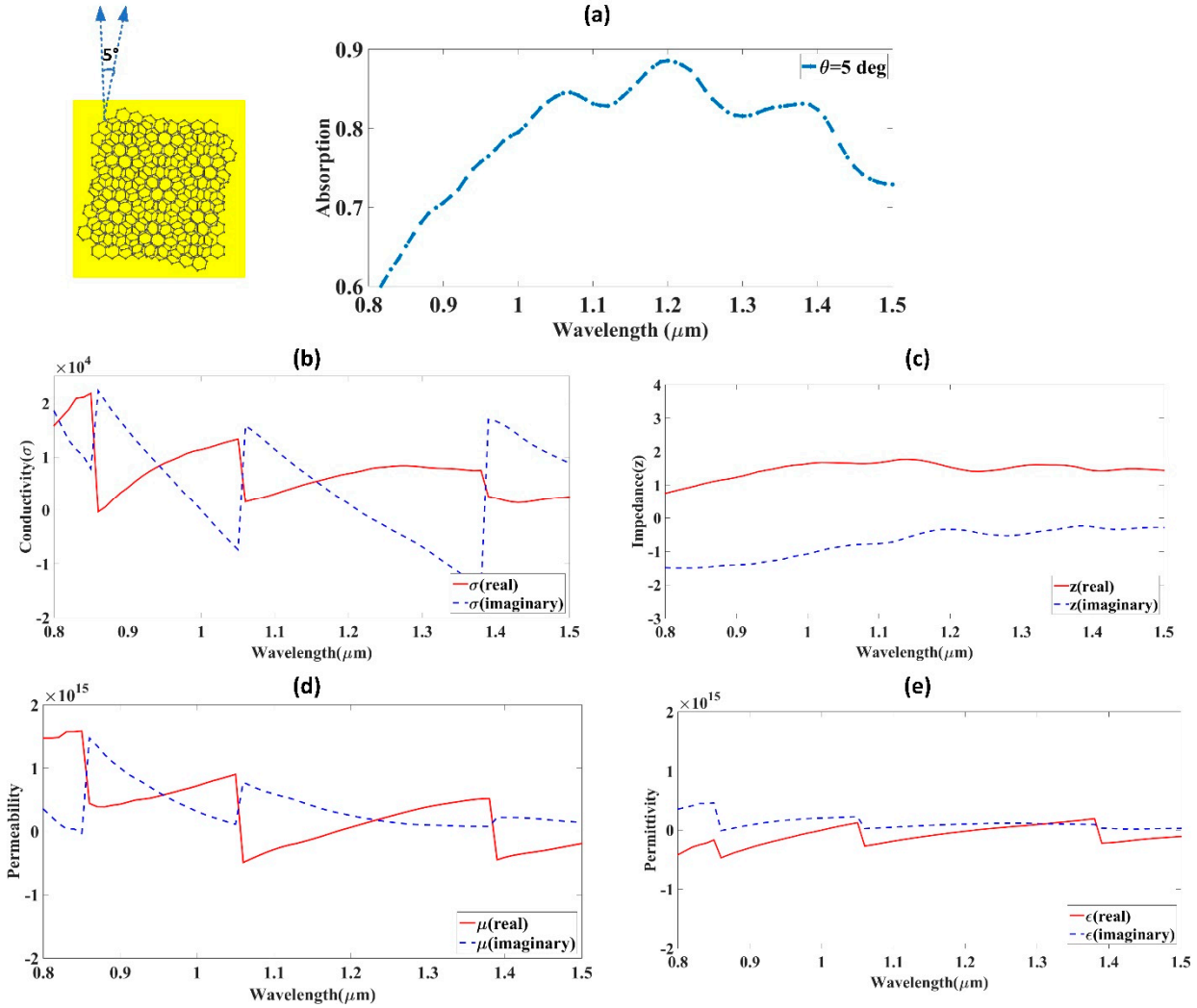

Figure 3. Bilayer graphene with twist angle of 5°. (**a**) Absorption; (**b**) conductivity (real (Re) and imaginary (Imag)); (**c**) impedance (Re and Imag); (**d**) permeability (Re and Imag); (**e**) permittivity (Re and Imag). The inset figure shows the schematic of bilayer graphene with a twist of 5°.

The response for twist angle 10° is provided in Figure 4. The response presented in the figure clearly shows the absorption response in Figure 4a, and its metamaterial properties, such as permittivity, permeability, conductivity, and impedance, are provided in other figures. The conductivity presented in Figure 4b shows that the imaginary part demonstrates two negative peaks at approximately 1.08 µm and 1.4 µm, while the real part demonstrates a negative peak of slightly less than 0 at approximately 0.85 µm. The impedance is presented in Figure 4c. The impedance values matched well with the real values of approximately 1 for the whole spectrum, and the imaginary values were less than 0 for most of the range. The two other important properties, namely, permittivity and permeability, are provided in Figure 4d,e, respectively. The real value of permeability

demonstrated negative peaks at apprxoimately 1.08 µm and 1.4 µm, providing the effect of the negative permeability of the metamaterial. The permittivity real values demonstrate negative peaks at approximately 0.88 µm, 1.08 µm, and 1.4 µm, demonstrating its metamaterial behavior for these wavelengths. Thus, the graphene twist of 10° demonstrates metamaterial behavior, with both its permittivity and permeability negative for 1.08 µm and 1.4 µm. Thus, the twist in the graphene layer demonstrates metamaterial behavior. As the twist angle increased, the negative behavior was also shifted in wavelength. Thus, the tuning was achieved using a change in twist angles for the metamaterial properties.

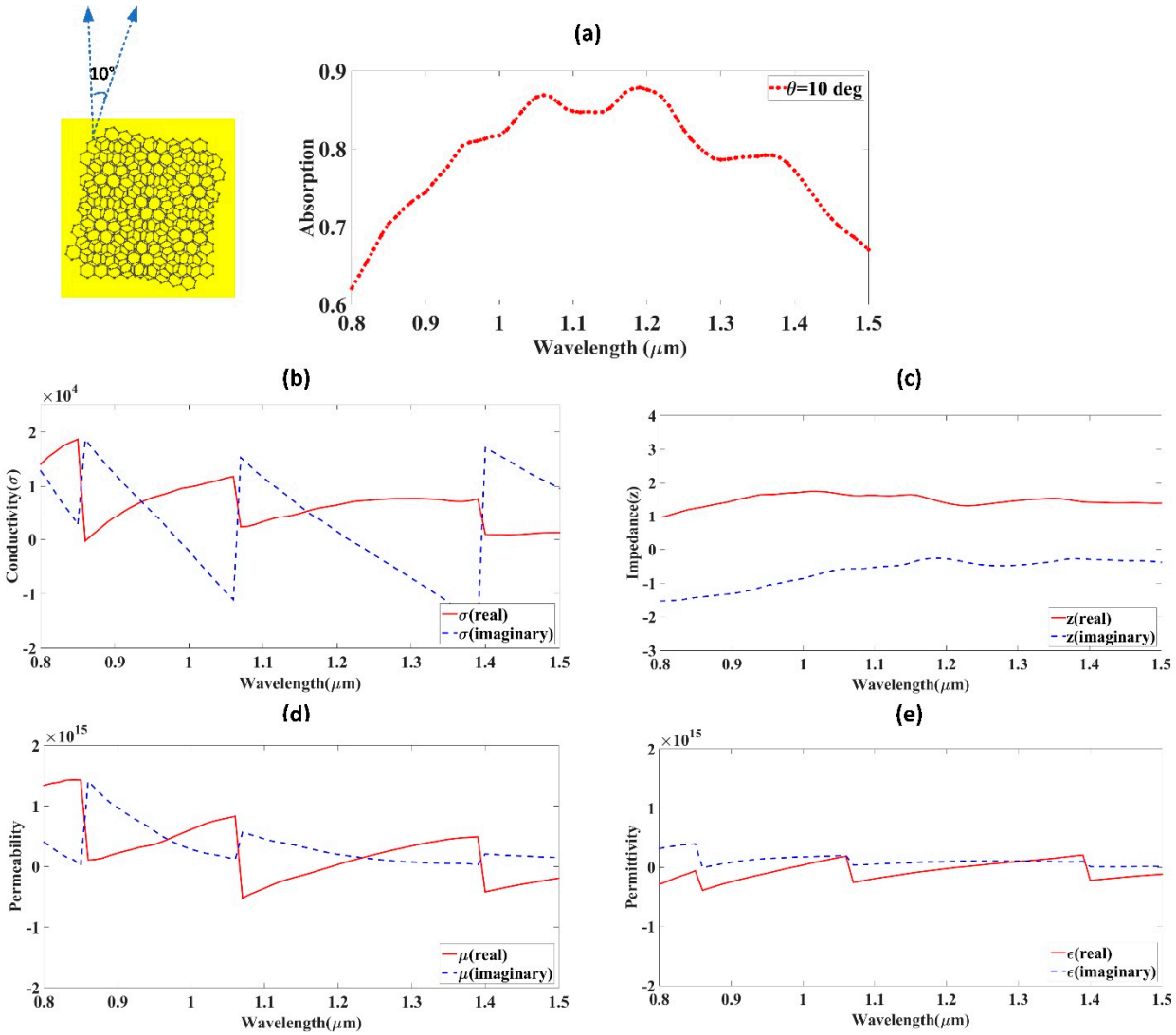

Figure 4. Bilayer graphene with twist angle of 10°. (**a**) Absorption; (**b**) conductivity (Re and Imag); (**c**) impedance (Re and Imag); (**d**) permeability (Re and Imag); (**e**) permittivity (Re and Imag). The inset figure shows the schematic of bilayer graphene with a twist of 10°.

The response of the graphene twist at 15° on the absorption and metamaterial properties is provided in Figure 6. As can be seen from the results, the negative values of the permittivity and permeability were available at wavelength around 0.88 µm, 1.08 µm, and 1.41 µm. As the twist angle increased, the negative behavior also shifted in wavelength. Thus, the tuning was achieved using a change in the twist angles for the metamaterial properties. This tuning behavior of the structure can be used for sensing different biomolecules with a high efficiency and sensitivity.

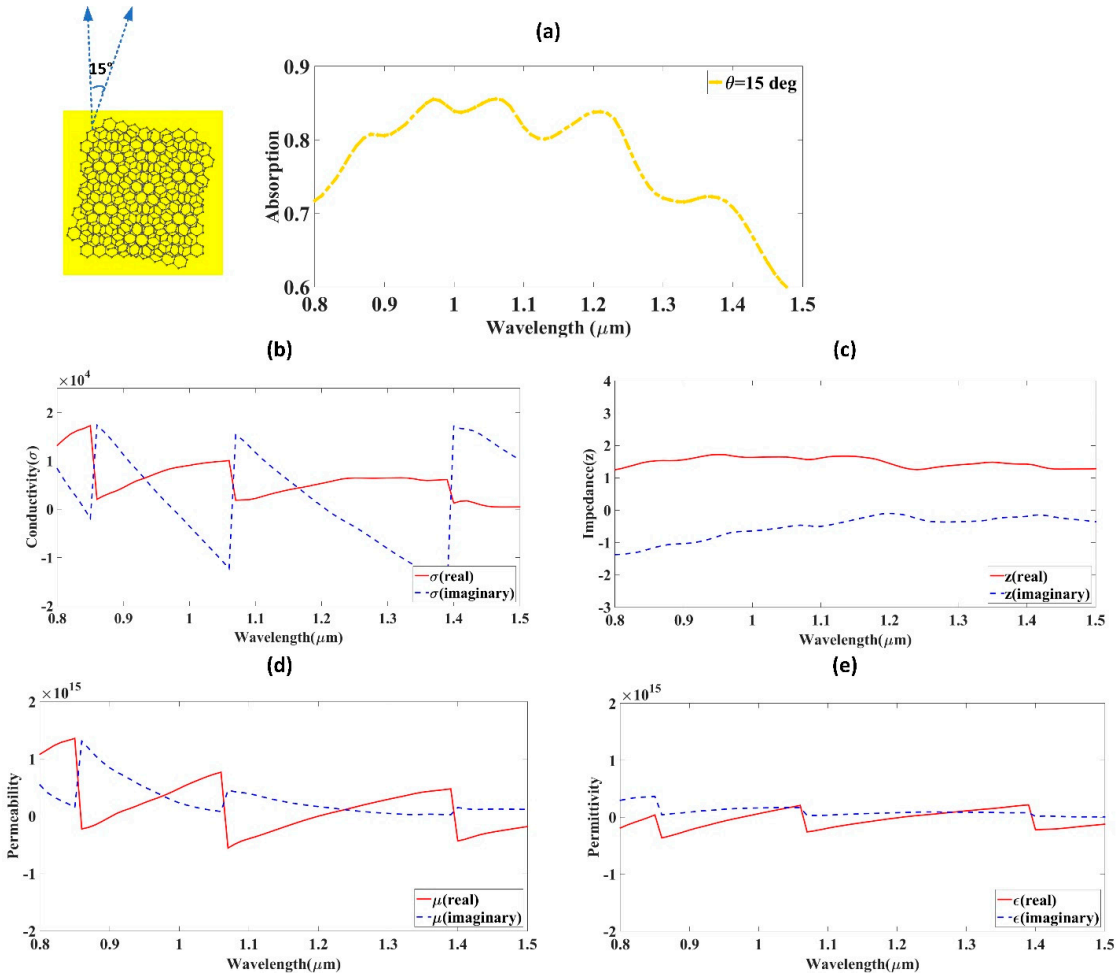

Figure 5. Bilayer graphene with twist angle of 15°. (**a**) Absorption; (**b**) conductivity (Re and Imag); (**c**) impedance (Re and Imag) (**d**) permeability (Re and Imag); (**e**) permittivity (Re and Imag). The inset figure shows the schematic of bilayer graphene with a twist of 15°.

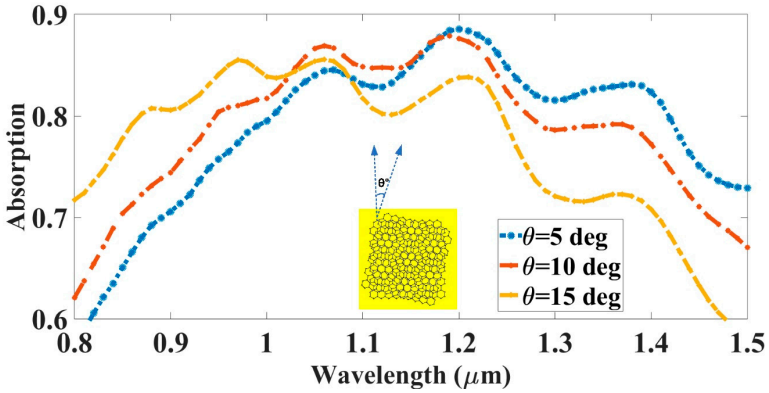

Figure 6. Comparison of absorption responses for three different twist angles (θ): 5°, 10°, and 15°. The tuning of the spectrum and wavelength peak is visible in the plot. The wavelength range is observed from 0.8 μm to 1.5 μm. The absorption is higher than 60% for the whole wavelength range.

A comparison of the absorption response for three twist angles, 5°, 10°, and 15°, is provided in Figure 6 and Table 1. The comparison clearly shows that the tuning of the wavelength is possible by changing the twist angles. The initial increase in the twist angle from 5° to 10° only shifted the absorption peak for a 10 nm wavelength. The increase in this twist from 10° to 15° shifted the absorption peak to 220 nm. This clearly shows that tuning

increases as the twist angle increases. The twisting presented for these different angles can be applicable for designing potentially tunable absorber devices as a maximum tuning of 220 nm was achieved in this design. The tuning presented in the table demonstrates that there is a potential for application in a tunable device in these graphene twistronics structures. The fabrication can be achieved by plying two monolayers of graphene structure separated by different angles.

Table 1. Tuning using twist angles.

Twist angles	5°	10°	15°
λ (μm)	1.2	1.19	0.97
Δλ (nm)	10		220

The angle of incidence of the light was varied to observe its effect on the twisted graphene layers. The response is presented in Figure 7. Here, nine different angles were observed with their absorption response. The absorption demonstrated a good response for all the angles except the 30 degree angle. The absorption for all the degrees showed a similar response, with only small variations which, in a way, indicate that the design is angle insensitive. Only for a small portion did the light decrease for the 30 degree angle. This could be because of the metamaterial effect achieved by twisting angles of the graphene layers. The results in the figure clearly show that there was almost more than 60% absorption for each angle for the range of 0.8 μm to 1.5 μm. This shows that the graphene twistronics design demonstrates a wide angle of incidence that can be applicable for many future absorption devices with these results. The wide angle of incidence also make it a potential candidate for different solar thermal energy devices.

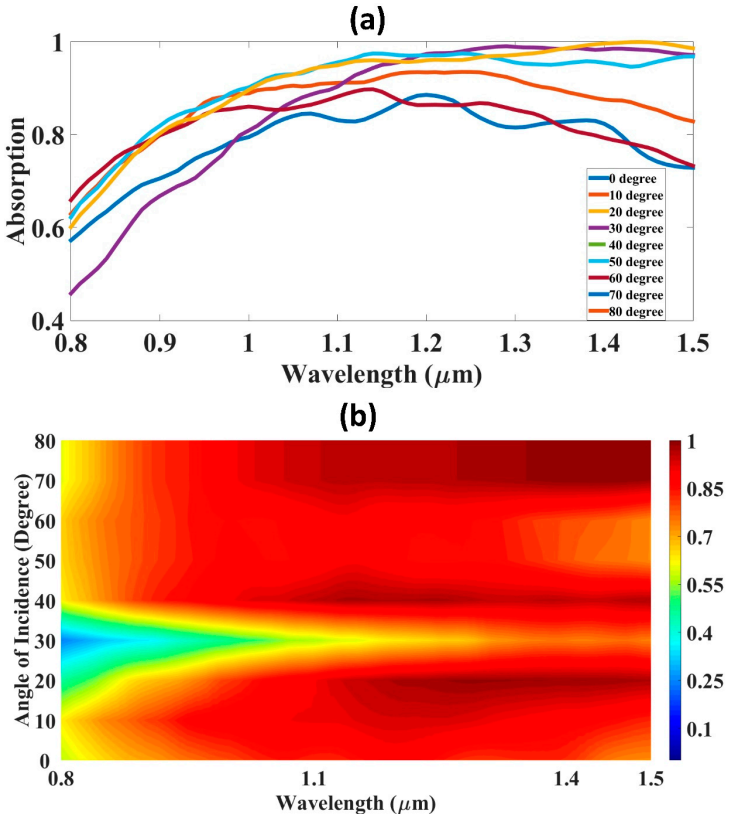

Figure 7. Absorption for variations in angle of incidence. (**a**) Plot indicating the absorption in 0 to 80 degrees. (**b**) Absorption for variations in wavelength and angle of incidence in which high absorption is indicated with a red color and low absorption is indicated with a blue color.

4. Machine Learning Prediction

Modern photonics devices frequently employ machine-learning-based algorithms for prediction. Many reliable mathematical techniques, such as the recurrent neural network, the convolutional neural network, the extra tree regression, etc., have been modified for this purpose [48–50]. A non-parametric, locally weighted linear regression (LWLR) learning algorithm will be used in this section [51]. We will examine the weighting function and the predicted function, and then use NumPy, Matplotlib, and seaborn to illustrate the predictions after first contrasting the parametric and non-parametric learning techniques. The best theta parameter values for parametric algorithms are sought during data training. In order to make future projections, we can completely rely on the parameterized model after determining the best values for these parameters, keeping in mind that the model serves a purpose as a whole. A non-parametric algorithm must store input data and model parameters permanently before it can produce predictions.

Due to the non-linear nature of the data, it is not possible to fit a straight line to the data as we would in a linear regression, which results in inaccurate predictions. A curved line must be fitted in order to achieve the smallest possible inaccuracy. When using an LWLR, we provide the model the location (x) at which we want to make a prediction. The model then provides that location's nearby $x^{(i)}$ a greater weight (closer to one) and the remaining $x^{(i)}$ a smaller weight (closer to zero). Finally, the model attempts to fit a straight line to the weighted $x^{(i)}$ values. This suggests that the model gives greater weight to the input data if the point is close to or around the circle and fits a straight line solely to the data that are close to or around the circle if we want to produce a forecast for a specific point on the x-axis. We will now go into detail about the weight distribution and circle size processes. The loss function ($J(\theta)$) for linear regression is as follows [51]:

$$J(\theta) = \sum_{i=1}^{m} \left(y^{(i)} - \theta^T x^{(i)} \right)^2 \tag{38}$$

The LWLR's modified loss function can be expressed as follows:

$$J(\theta) = \sum_{i=1}^{m} w^{(i)} \left(y^{(i)} - \theta^T x^{(i)} \right)^2 \tag{39}$$

where $w^{(i)}$ is the weight of the ith training example, and it can be given as:

$$w^{(i)} = exp\left(-\frac{\left(x^{(i)} - x \right)^T \left(x^{(i)} - x \right)}{2} \right) \tag{40}$$

There will be a prediction in the case of x. To identify the ith training exercise that has been finished, use the notation $x^{(i)}$. This function's value can neither rise above one nor fall below zero. Consequently, $2^{(i)}$ is very close to the number 1 when the difference between x and $x^{(i)}$ is quite small, as can be seen by looking at the function $\left| x^{(i)} - x \right|$. When $\left| x^{(i)} - x \right|$ is close to zero, $w^{(i)}$ is also close to zero. For $x^{(i)}$ values that are particularly far away from x, $w^{(i)}$ is very near to 0, but it is very close to 1 for $x^{(i)}$ values that are abnormally close to x. As a result, for values of $x^{(i)}$ that are very close to x, the error components in the loss function are raised by virtually one, and for values of $x^{(i)}$ that are extremely far from x, they are practically nil. For the addition of the error terms, only the values of $x^{(i)}$ that are reasonably close to x are taken into account.

We employ a weighting function that has a hyperparameter symbolized by the symbol tau (τ) to determine the circle's radius. Circle diameters can be changed to be wider or narrower by adjusting the hyperparameter's value. The formula for computing the

modified weight can now be written as follows, which also refers to the range over which the weighing function's Gaussian bell-shaped curve varies:

$$w^{(i)} = exp\left(-\frac{\left(x^{(i)} - x\right)^T\left(x^{(i)} - x\right)}{2\tau^2}\right) \tag{41}$$

The following formula can be used to determine the value of the parameter theta immediately, without using model training, because there is a closed-form solution available for this technique.

$$\theta = \left(X^T W X\right)^{-1}\left(X^T W Y\right) \tag{42}$$

Using the formula below, we can make predictions after knowing the value of theta:

$$\theta^T x \tag{43}$$

The predictive ability of the regression model is assessed using the R^2 score, which may be computed using Equation (19).

$$R^2 = 1 - \frac{\sum_{i=1}^{N}(Predicted\ Value_i - ActualValue_i)^2}{\sum_{i=1}^{N}(ActualValue_i - AverageValue\ )^2} \tag{44}$$

An absorption prediction was carried out for different twist angles, and the impact of hyperparameter τ on the absorption prediction was also investigated. The detailed results with a heatmap are provided in Figure 8. For this particular study, the hyperparameter, τ was varied for three values, i.e., 0.02, 0.2, and 2. The results make it abundantly evident that the capability of the LWLR model to predict the intermediate values with a high accuracy declines when the hyperparameter τ is increased. This, in turn, results in a lower R^2 score. For τ = 0.02, we achieved the near-unity R^2 score, indicating the high performance of the model, as shown in Figure 8a,d,g. When we increase the hyperparameter to 0.2, the R^2 score decreases slightly but still yields a high performance, as shown in Figure 8b,e,h and indicated by the R^2 score in the range of 0.9914 to 0.9928. However, when we set τ equal to 2, the whole picture shifts, as can be seen in Figure 8c,f,i in which the actual values compared to the anticipated values vary widely. The accuracy of the prediction is also influenced by this, as is shown in the heatmap displayed in Figure 8j.

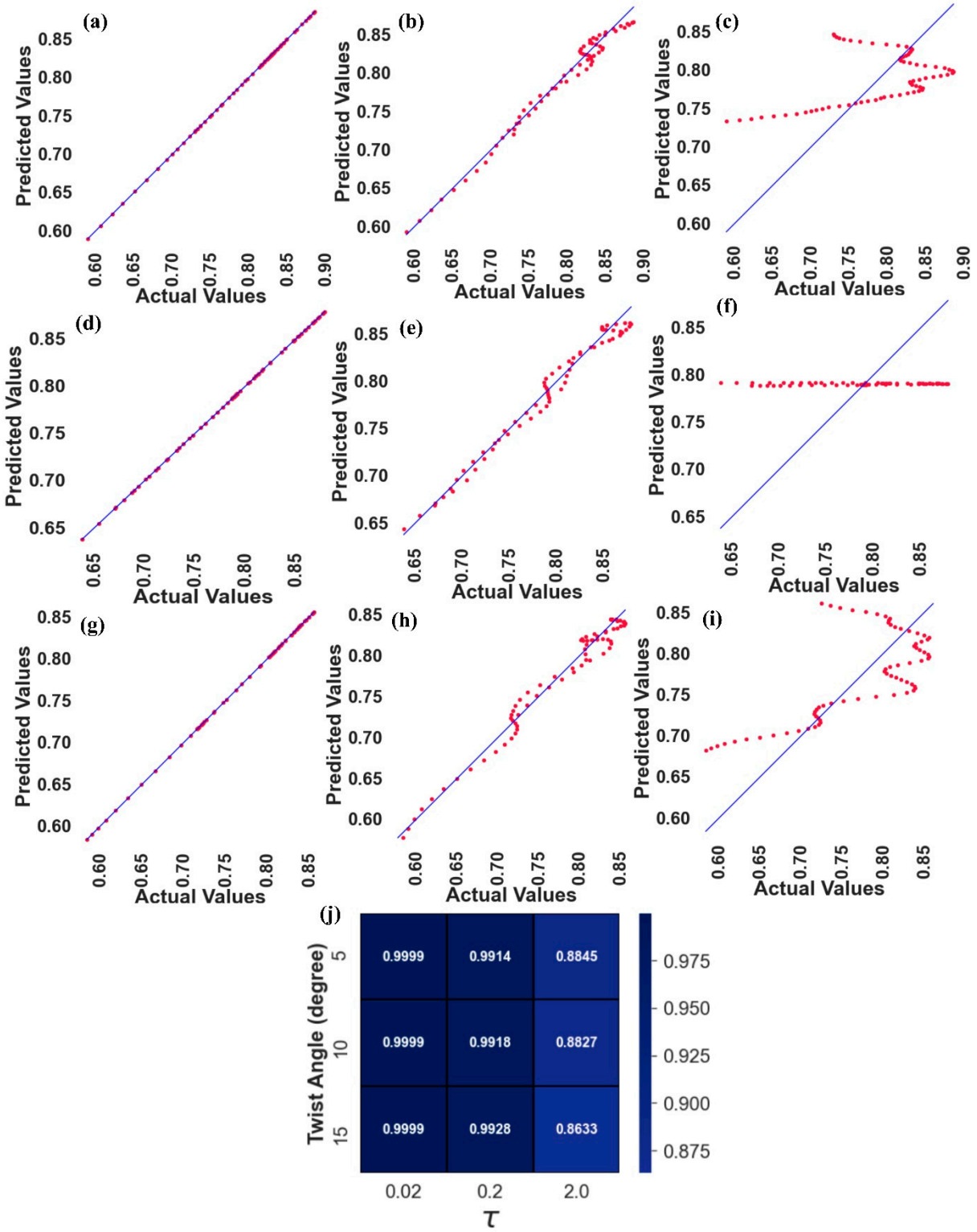

Figure 8. Actual vs. predicted values of absorption for different values of twist angle and hyper-parameter: (**a**) for twist angle = 5° and τ = 0.02, (**b**) for twist angle = 5° and τ = 0.2, (**c**) for twist angle = 5° and τ = 2, (**d**) for twist angle = 10° and τ = 0.02, (**e**) for twist angle = 10° and τ = 0.2, (**f**) for twist angle = 10° and τ = 2, (**g**) for twist angle = 15° and τ = 0.02, (**h**) for twist angle = 15 and τ = 0.2, and (**i**) for twist angle = 15° and τ = 2. (**j**) Heatmap depicting higher prediction accuracy for τ = 0.02; as we increase it to 2, prediction accuracy drops.

5. Conclusions

A novel numerical approach for using graphene material was analyzed, and a metamaterial effect was achieved in this research. We proposed a new graphene twistronics concept to achieve tuning in the absorption spectrum. Small-angle twists of 5°, 10°, and 15° were applied to a bilayer graphene material. The twist in the angle tuned the absorption result. The peak of absorption shifted from 10 nm to 220 nm for different angle twists. A twist with a higher degree angles decreased the conductivity values. The twisted graphene layers also demonstrated negative permittivity and negative permeability, similar to metamaterials. The metamaterial-like properties of the low-cost graphene material, which has transparency and flexibility, can pave the way for new photovoltaic applications. This research opens a new door for research on graphene material and metamaterials. Using an LWLR analysis, we estimated the absorption values for intermediate/missing wavelength values. Using the hyperparameter $\tau = 0.02$, we acquired an R^2 score of 0.9999, indicating the model's strong performance.

Author Contributions: Conceptualization, A.A. and S.K.P.; methodology, A.A and S.K.P.; software, M.A., K.A., O.A., and A.A.; Investigation, J.P.; writing—original draft preparation, all authors; writing—review and editing, A.A. and S.K.P. All authors have read and agreed to the published version of the manuscript.

Funding: Researchers Supporting Project number (RSPD2023R654), King Saud University, Riyadh, Saudi Arabia.

Data Availability Statement: The data will be made available upon reasonable request to the corresponding author.

Acknowledgments: Researchers Supporting Project number (RSPD2023R654), King Saud University, Riyadh, Saudi Arabia.

Conflicts of Interest: The authors declare no conflict of interest.

Nomenclature

v	Dirac Velocity
k	momentum measured from the layer's Dirac point
θ_k	momentum orientation relative to the x axis
Ω	unit cell area
t_q	Fourier transform of the tunneling amplitude t(r)
G_1, G_2	Summed over reciprocal lattice vectors
Ψ_0	one of the two zero energy state of $\Psi_0^{(1)}$ and $\Psi_0^{(2)}$ of the isolated layer
σ_{CF}	Counterflow conductivity
v^*	Density Of States of the twisted bilayer
T	Temperature
r	Reflectance
θ	Angle of incidence

References

1. Geim, A.K.; Novoselov, K.S. The Rise of Graphene. *Nat. Mater.* **2007**, *6*, 183–191. [CrossRef]
2. Patel, S.K.; Surve, J.; Parmar, J.; Natesan, A.; Katkar, V. Graphene-Based Metasurface Refractive Index Biosensor For Hemoglobin Detection: Machine Learning Assisted Optimization. *IEEE Trans. Nanobioscience* **2022**. [CrossRef] [PubMed]
3. Patel, S.K.; Surve, J.; Parmar, J.; Armghan, A.; Aliqab, K.; Altahan, B.R.; Ahmed, K.; Bui, F.M.; Al-Zahrani, F.A. Graphene-Based H-Shaped Biosensor with High Sensitivity and Optimization Using ML-Based Algorithm. *Alex. Eng. J.* **2023**, *68*, 15–28. [CrossRef]
4. Khan, M.E.; Khan, M.M.; Cho, M.H. Recent Progress of Metal-Graphene Nanostructures in Photocatalysis. *Nanoscale* **2018**, *10*, 9427–9440. [CrossRef] [PubMed]
5. Qi, Y.; Liu, C.; Hu, B.; Deng, X.; Wang, X. Tunable Plasmonic Absorber in THz-Band Range Based on Graphene "Arrow" Shaped Metamaterial. *Results Phys.* **2019**, *15*, 102777. [CrossRef]
6. Patel, S.K.; Surve, J.; Parmar, J.; Aliqab, K.; Alsharari, M.; Armghan, A. SARS-CoV-2 Detecting Rapid Metasurface-Based Sensor. *Diam. Relat. Mater.* **2023**, *132*, 109644. [CrossRef]

7. Olabi, A.G.; Abdelkareem, M.A.; Wilberforce, T.; Sayed, E.T. Application of Graphene in Energy Storage Device—A Review. *Renew. Sustain. Energy Rev.* **2020**, *135*, 110026. [CrossRef]
8. Fardoost, A.; Vanani, F.G.; Amirhosseini, A.; Safian, R. Design of a Multilayer Graphene-Based Ultrawideband Terahertz Absorber. *IEEE Trans. Nanotechnol.* **2017**, *16*, 68–74. [CrossRef]
9. Cen, C.; Chen, Z.; Xu, D.; Jiang, L.; Chen, X.; Yi, Z.; Wu, P.; Li, G.; Yi, Y. High Quality Factor, High Sensitivity Metamaterial Graphene—Perfect Absorber Based on Critical Coupling Theory and Impedance Matching. *Nanomaterials* **2020**, *10*, 95. [CrossRef]
10. Rahmanshahi, M.; Noori Kourani, S.; Golmohammadi, S.; Baghban, H.; Vahed, H. A Tunable Perfect THz Metamaterial Absorber with Three Absorption Peaks Based on Nonstructured Graphene. *Plasmonics* **2021**, *16*, 1665–1676. [CrossRef]
11. Patel, S.K.; Charola, S.; Parmar, J.; Ladumor, M.; Ngo, Q.M.; Dhasarathan, V. Broadband and Efficient Graphene Solar Absorber Using Periodical Array of C-Shaped Metasurface. *Opt. Quantum Electron.* **2020**, *52*, 250. [CrossRef]
12. Ogawa, S.; Shimatani, M.; Fukushima, S.; Okuda, S.; Matsumoto, K. Graphene on Metal-Insulator-Metal-Based Plasmonic Metamaterials at Infrared Wavelengths. *Opt. Express* **2009**, *26*, 5665–5674. [CrossRef] [PubMed]
13. Patel, S.K.; Parmar, J.; Katkar, V. Graphene-Based Multilayer Metasurface Solar Absorber with Parameter Optimization and Behavior Prediction Using Long Short-Term Memory Model. *Renew. Energy* **2022**, *191*, 47–58. [CrossRef]
14. Muhammad, N.; Tang, X.; Tao, F.; Qiang, L.; Zhengbiao, O. Broadband Polarization-Insensitive Absorption by Metasurface with Metallic Pieces for Energy Harvesting Application. *Mater. Sci. Eng. B Solid-State Mater. Adv. Technol.* **2019**, *249*, 114419. [CrossRef]
15. Poorgholam-Khanjari, S.; Zarrabi, F.B. Reconfigurable Vivaldi THz Antenna Based on Graphene Load as Hyperbolic Metamaterial for Skin Cancer Spectroscopy. *Opt. Commun.* **2021**, *480*, 126482. [CrossRef]
16. Xu, Z.; Dong, X.; Bornemann, J. Design of a Reconfigurable MIMO System for THz Communications Based on Graphene Antennas. *IEEE Trans. Terahertz Sci. Technol.* **2014**, *4*, 609–617. [CrossRef]
17. Lucido, M. Electromagnetic Scattering from a Graphene Disk: Helmholtz-Galerkin Technique and Surface Plasmon Resonances. *Mathematics* **2021**, *9*, 1429. [CrossRef]
18. Frieler, M.; Pho, C.; Lee, B.H.; Dobrovolny, H.; Naumov, A.V.; Akkaraju, G.R. Effects of Doxorubicin Delivery by Nitrogen-Doped Graphene Quantum Dots on Cancer Cell Growth: Experimental Study and Mathematical Modeling. *Nanomaterials* **2021**, *11*, 140. [CrossRef]
19. Carr, S.; Massatt, D.; Fang, S.; Cazeaux, P.; Luskin, M.; Kaxiras, E. Twistronics: Manipulating the Electronic Properties of Two-Dimensional Layered Structures through Their Twist Angle. *Phys. Rev. B* **2017**, *95*, 075420. [CrossRef]
20. Yang, Y.; Li, J.; Yin, J.; Xu, S.; Mullan, C.; Taniguchi, T.; Watanabe, K.; Geim, A.K.; Novoselov, K.S.; Mishchenko, A. In Situ Manipulation of van Der Waals Heterostructures for Twistronics. *Sci. Adv.* **2020**, *6*, eabd3655. [CrossRef]
21. Andrei, E.Y.; MacDonald, A.H. Graphene Bilayers with a Twist. *Nat. Mater.* **2020**, *19*, 1265–1275. [CrossRef]
22. Weckbecker, D.; Shallcross, S.; Fleischmann, M.; Ray, N.; Sharma, S.; Pankratov, O. Low-Energy Theory for the Graphene Twist Bilayer. *Phys. Rev. B* **2016**, *93*, 035452. [CrossRef]
23. Mogera, U.; Kulkarni, G.U. A New Twist in Graphene Research: Twisted Graphene. *Carbon N. Y.* **2020**, *156*, 470–487. [CrossRef]
24. Ren, Y.N.; Zhang, Y.; Liu, Y.W.; He, L. Twistronics in Graphene-Based van Der Waals Structures. *Chin. Phys. B* **2020**, *29*, 117303. [CrossRef]
25. Wu, D.; Pan, Y.; Min, T. Twistronics in Graphene, from Transfer Assembly to Epitaxy. *Appl. Sci.* **2020**, *10*, 4690. [CrossRef]
26. Liao, M.; Wei, Z.; Du, L.; Wang, Q.; Tang, J.; Yu, H.; Wu, F.; Zhao, J.; Xu, X.; Han, B.; et al. Precise Control of the Interlayer Twist Angle in Large Scale MoS_2 Homostructures. *Nat. Commun.* **2020**, *11*, 2153. [CrossRef]
27. Hu, G.; Qiu, C.-W.; Alù, A. Twistronics for Photons: Opinion. *Opt. Mater. Express* **2021**, *11*, 1377. [CrossRef]
28. Deng, Y.; Oudich, M.; Gerard, N.J.R.K.; Ji, J.; Lu, M.; Jing, Y. Magic-Angle Bilayer Phononic Graphene. *Phys. Rev. B* **2020**, *102*, 180304. [CrossRef]
29. Ciarrocchi, A.; Tagarelli, F.; Avsar, A.; Kis, A. Excitonic Devices with van Der Waals Heterostructures: Valleytronics Meets Twistronics. *Nat. Rev. Mater.* **2022**, *7*, 449–464. [CrossRef]
30. Peng, J.; Zhao, L.; Zhao, T. Study on Dynamic Characteristics of a Rotating Sandwich Porous Pre-Twist Blade with a Setting Angle Reinforced by Graphene Nanoplatelets. *Mathematics* **2022**, *10*, 2814. [CrossRef]
31. Li, H.; Liu, H.; Zou, J. Minnaert Resonances for Bubbles in Soft Elastic Materials. *SIAM J. Appl. Math.* **2022**, *82*, 119–141. [CrossRef]
32. Deng, Y.; Liu, H.; Zheng, G.H. Mathematical Analysis of Plasmon Resonances for Curved Nanorods. *J. Math. Pures Appl.* **2021**, *153*, 248–280. [CrossRef]
33. Zheng, G.H. Mathematical Analysis of Plasmonic Resonance for 2-D Photonic Crystal. *J. Differ. Equ.* **2019**, *266*, 5095–5117. [CrossRef]
34. Li, H. Recent Progress On The Mathematical Study Of Anomalous Localized Resonance In Elasticity. *Electron. Res. Arch.* **2020**, *28*, 1257–1272. [CrossRef]
35. Wang, S.; Ren, C.; Tian, H.; Yu, J.; Sun, M. MoS_2/ZnO van Der Waals Heterostructure as a High-Efficiency Water Splitting Photocatalyst: A First-Principles Study. *Phys. Chem. Chem. Phys.* **2018**, *20*, 13394–13399. [CrossRef]
36. Wang, S.; Tian, H.; Ren, C.; Yu, J.; Sun, M. Electronic and Optical Properties of Heterostructures Based on Transition Metal Dichalcogenides and Graphene-like Zinc Oxide. *Sci. Rep.* **2018**, *8*, 12009. [CrossRef] [PubMed]
37. COMSOL. *COMSOL Multiphysics®*, version 6.0; COMSOL: Stockholm, Sweden, 2021.
38. Niu, K.; Li, P.; Huang, Z.; Jiang, L.J.; Bagci, H. Numerical Methods for Electromagnetic Modeling of Graphene: A Review. *IEEE J. Multiscale Multiphysics Comput. Tech.* **2020**. [CrossRef]

39. Bludov, Y.V.; Ferreira, A.; Peres, N.M.R.; Vasilevskiy, M.I. A Primer on Surface Plasmon-Polaritons in Graphene. *Int. J. Mod. Phys. B* **2013**. [CrossRef]
40. Kouroublakis, M.; Tsitsas, N.L.; Fikioris, G. Shielding Effectiveness of Ideal Monolayer Graphene in Cylindrical Configurations With the Method of Auxiliary Sources. *IEEE Trans. Electromagn. Compat.* **2022**, *64*, 1042–1051. [CrossRef]
41. Surve, J.; Parmar, J.; Patel, S.K.; Jadeja, R. Comparative Analysis of Metasurface Array-Based Solar Absorber for Visible Region. *Opt. Quantum Electron.* **2021**, *53*, 696. [CrossRef]
42. Gusynin, V.P.; Sharapov, S.G.; Carbotte, J.P. Magneto-Optical Conductivity in Graphene. *J. Phys. Condens. Matter* **2007**, *19*, 026222. [CrossRef]
43. Castro Neto, A.H.; Guinea, F.; Peres, N.M.R.; Novoselov, K.S.; Geim, A.K. The Electronic Properties of Graphene. *Rev. Mod. Phys.* **2009**, *81*, 109–162. [CrossRef]
44. Bistritzer, R.; MacDonald, A.H. Moiré Bands in Twisted Double-Layer Graphene. *Proc. Natl. Acad. Sci. USA* **2011**, *108*, 12233–12237. [CrossRef]
45. Numan, A.B.; Sharawi, M.S. Extraction of Material Parameters for Metamaterials Using a Full-Wave Simulator [Education Column]. *IEEE Antennas Propag. Mag.* **2013**, *55*, 202–221. [CrossRef]
46. Azad, A.K.; Kort-Kamp, W.J.M.; Sykora, M.; Weisse-Bernstein, N.R.; Luk, T.S.; Taylor, A.J.; Dalvit, D.A.R.; Chen, H.T. Metasurface Broadband Solar Absorber. *Sci. Rep.* **2016**, *6*, 20347. [CrossRef]
47. Mahmud, S.; Islam, S.S.; Almutairi, A.F.; Islam, M.T. A Wide Incident Angle, Ultrathin, Polarization-Insensitive Metamaterial Absorber for Optical Wavelength Applications. *IEEE Access* **2020**, *8*, 129525–129541. [CrossRef]
48. Patel, S.K.; Surve, J.; Katkar, V.; Parmar, J.; Al-Zahrani, F.A.; Ahmed, K.; Bui, F.M. Encoding and Tuning of THz Metasurface-Based Refractive Index Sensor with Behavior Prediction Using XGBoost Regressor. *IEEE Access* **2022**, *10*, 24797–24814. [CrossRef]
49. Patel, S.K.; Surve, J.; Katkar, V.; Parmar, J. Optimization of Metamaterial-Based Solar Energy Absorber for Enhancing Solar Thermal Energy Conversion Using Artificial Intelligence. *Adv. Theory Simul.* **2022**, *5*, 2200139. [CrossRef]
50. Patel, S.K.; Surve, J.; Jadeja, R.; Katkar, V.; Parmar, J.; Ahmed, K. Ultra-Wideband, Polarization-Independent, Wide-Angle Multilayer Swastika-Shaped Metamaterial Solar Energy Absorber with Absorption Prediction Using Machine Learning. *Adv. Theory Simul.* **2022**, *5*, 2100604. [CrossRef]
51. Cleveland, W.S.; Devlin, S.J. Locally Weighted Regression: An Approach to Regression Analysis by Local Fitting. *J. Am. Stat. Assoc.* **1988**, *83*, 596–610. [CrossRef]